ACS OMEGA

http://pubs.acs.org/journal/acsodf

Article

Optimization Analysis of Particle Separation Parameters for a Standing Surface Acoustic Wave Acoustofluidic Chip

Junlong Han, Hong Hu,* Yulin Lei, Qingyun Huang, Chen Fu,* Chenhui Gai, and Jia Ning

Cite This: *ACS Omega* 2023, 8, 311−323

Read Online

ACCESS | Metrics & More | Article Recommendations | Supporting Information

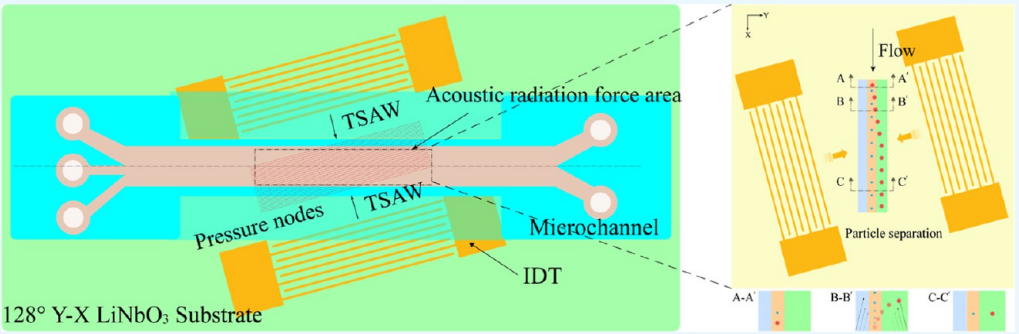

ABSTRACT: Microparticle separation technology is an important technology in many biomedical and chemical engineering applications from sample detection to disease diagnosis. Although a variety of microparticle separation techniques have been developed thus far, surface acoustic wave (SAW)-based microfluidic separation technology shows great potential because of its high throughput, high precision, and integration with polydimethylsiloxane (PDMS) microchannels. In this work, we demonstrate an acoustofluidic separation chip that includes a piezoelectric device that generates tilted-angle standing SAWs and a permanently bonded PDMS microchannel. We established a mathematical model of particle motion in the microchannel, simulated the particle trajectory through finite element simulation and numerical simulation, and then verified the validity of the model through acoustophoresis experiments. To improve the performance of the separation chip, the influences of particle size, flow rate, and input power on the particle deflection distance were studied. These parameters are closely related to the separation purity and separation efficiency. By optimizing the control parameters, the separation of micron and submicron particles under different throughput conditions was achieved. Moreover, the separation samples were quantitatively analyzed by digital light scattering technology and flow cytometry, and the results showed that the maximum purity of the separated particles was ∼95%, while the maximum efficiency was ∼97%.

1. INTRODUCTION

In many biological and medical applications, the efficient separation of particles or cells based on microfluidic approaches provides a convenient, miniaturized, automated, and reliable method for disease diagnosis,[1−3] drug screening,[4,5] and cell analysis.[6−8] The microfluidic technology is also called lab-on-a-chip. Through the design of ingenious microchannel structures and actuators, the entire cell and particle separation process can be scaled down to a small chip. Based on the differences in physical and biological characteristics between the target particles or cells and other components in the sample, multiple technologies can be utilized to develop such separation technologies. To date, a variety of separation technologies have been developed, including microfiltration,[9] deterministic lateral displacement,[10] inertial microfluidics,[11] pinched flow fractionation,[12] hydrodynamic filtration,[13] dielectrophoresis,[14] optofluidics,[14] magnetophoresis,[16] and acoustofluidics,[17−19] as comprehensively reviewed by Hoorfar's,[20] Lenshof's, and Laurell's groups.[21,22]

Acoustophoresis usually refers to the displacement behavior of particles or cells subjected to acoustic waves and streaming in microfluidics. It is a potentially active method for the separation of particles or cells.[15] The piezoelectric transducer (PET) or interdigital transducer (IDT) is introduced as the actuator to generate the acoustic pressure field, and the particles suspended in the microflow field are affected by both the acoustic radiation force (ARF) and the acoustic streaming flow (ASF) when exposed to acoustic waves.[23−25] By controlling the physical properties of the fluid and acoustics, such as density,[26] compressibility,[27,28] size,[29] acoustic

Received: July 17, 2022
Accepted: December 19, 2022
Published: December 27, 2022

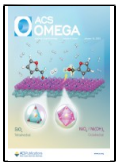

https://doi.org/10.1021/acsomega.2c04273
ACS Omega 2023, 8, 311−323

frequency,[30] and acoustic pressure amplitude,[31] the separation of particles with different physical properties can be achieved in accordance with different motion responses arising from the particles in the acoustic pressure field. In addition, acoustophoresis exerts almost no or a very slight influence on cell viability and function, which also makes it more readily acceptable for implementation in medical engineering.[32−34] Since the development of soft lithography technology, microfluidic channels with polydimethylsiloxane (PDMS) as the main material have been widely used in microfluidic devices and can be integrated on the surface of glass and piezoelectric crystals, which is of great significance for the miniaturization and integration of microfluidic chips.

To date, acoustic-driven particle separation microfluidic systems mainly use bulk acoustic waves (BAWs) or surface acoustic waves (SAWs).[35−38] The BAW microfluidic systems usually prepare microchannels on a glass substrate or silicon substrate in advance. BAWs are excited within volumes of fluid by mounting a composite PET (e.g., lead zirconate titanate) next to the microchannel, operating at a frequency that is generally less than 10 MHz and corresponding to the resonance mode in the fluid volume. Contrary to the BAW microfluidic system, the SAW microfluidic system first needs to prepare SAW devices. SAWs are generated by a set of interdigital electrodes sputtered on the surface of a piezoelectric substrate, and the frequency can reach several hundred megahertz. Afterward, the surface of the device is bonded with microchannels by oxygen plasma treatment. In contrast to BAWs, fluid resonance is not excited; hence, the suspended particles in the microchannel can be manipulated more flexibly by methods including particle sorting,[39] particle patterning,[40] and particle filtration.[38]

In SAW-driven devices, acoustic waves that radiate away from the IDT are termed travelling SAWs (TSAWs). Standing SAWs (SSAWs) are generated when two oppositely propagating TSAWs or a single TSAW reflected from a sound hard boundary constructively interferes, resulting in the formation of regions of minimum and maximum pressure fluctuations, known as time-averaged pressure nodes (PNs) and pressure anti-nodes (PAs), respectively. In the SSAW field, the ARF collects the suspended particles to the node or anti-node, which is determined according to the acoustic contrast factor between the particle and the host fluid. However, a set of frequency-matched IDTs are usually used to establish a strong periodic acoustic pressure field across the width of the channel due to the inherent attenuation in SAW propagation. As with BAW, the dominant particle manipulation mechanism has a size dependency whether it involves patterning, sorting, or concentrating, which results in the particle position change across the width of the channel.

In recent years, there have been an increasing number of studies on SSAW-based particle sorting.[34,41] In the traditional design, in order to set the position of the PN line in the laminar flow of the fluid domain at the particle collection outlet, it is necessary to match the wavelength of the SSAW device with the width of the microchannel.[42,43] This complicates system design, requires high-precision alignment of the microchannel with the SSAW device, and limits particle sorting throughput. Meanwhile, a series of recent studies have observed the existence of an "anechoic corner" within the channel.[44] This region is located along the edge of the channel closest to the source. In this area, the acoustic pressure is weak and accompanied by strong streaming. As the SSAW is coupled to the fluid volume, some particles are affected by the "anechoic corner" and will be pushed to the edge of the channel instead of being collected at PNs or PAs. However, Huang's research group circumvented this limitation, demonstrating that an SSAW acoustofluidic system with a tilt angle can solve the above problems.[45−48] For example, Ding et al. isolated MCF-7 epithelial cancer cells from healthy human leukocytes based on the taSSAW system with an isolation purity of up to 84%.[49] Li et al. demonstrated that the taSSAW method can efficiently isolate circulating tumor cells from leukocytes with isolation purity as high as 84−96%.[50] In addition, Wu et al. demonstrated acoustic-based high-throughput particle separation in continuous flow with the taSSAW system with flow rates up to 500 μL/min.[51] Although high recovery and high throughput are confirmed in the experimental results, the parameter optimization method to improve the separation purity and the study of flow rate and acoustic intensity with respect to the separation of submicron particles in the permanent bonding channel have not been considered in the relevant experiment.

In this work, we propose a direct-type IDT-based taSSAW chip for the separation of micron particles and submicron particles in a continuous flow. Unlike the detachable and dual-inlet microchannel, we used a triple-inlet microchannel with a titled angle, which is permanently bonded. To combine the PDMS microchannel and the taSSAW chip more firmly, we sputtered a layer of SiO_2 film on the taSSAW chip. Particles of four different sizes are precisely deflected into distinguishable streams, demonstrating the controllability of the acoustofluidic platform. We achieved the separation of different particles ranging in size from 100 nm to 6 μm, including 1 μm PS particles and 3 μm PS particles, 1 μm PS particles and 6 μm PS particles, 100 nm PS particles and 1 μm PS particles, and 100 nm PS particles and 750 nm SiO_2 particles. In addition, we performed particle size analysis of the separated particles using digital light scattering (DLS) techniques and counted particles using flow cytometry. The results showed that the particle separation by this platform achieved high particle purity with good efficiency. For the physical principle of acoustic separation, we established a two-dimensional (2D) physical model of the acoustic streaming field in the microchannel through finite element simulation and further elaborated the dominant mechanisms of ARF and ASF. The particle trajectories were predicted by numerical simulation and finally the validity of the model was verified by experiments. Compared with previously reported studies on the separation of microparticles and particles, we added a physical explanation of particle streaming vortices and particle linearization phenomena in microchannels and the correlation of particle trajectories with device input power and flow rate. The SAW device uses a direct-type IDT rather than a design with a reflective grid. The number of finger pairs can be used to adjust the impedance of the SAW device.[52] We believe that, by virtue of the device's label-free, high integration, and contactless advantages, the taSSAW-based separation device can facilitate the development of acoustofluidics in point-of-care testing systems.

2. MATERIALS AND METHODS

2.1. Device Fabrication. The bidirectional IDT-based acoustofluidic chip consists of a pair of identical SAW transducers and microchannels, as shown in Figure 1A. Two major steps were involved in the fabrication of the taSSAW

https://doi.org/10.1021/acsomega.2c04273
ACS Omega 2023, 8, 311−323

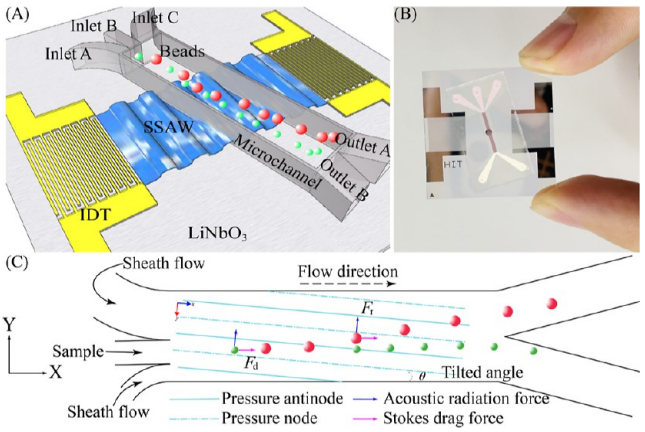

Figure 1. (A) Schematic and (B) photograph of the acoustofluidic separation chip using the taSSAW-based design. (C) Schematic of the working mechanism of taSSAW-based particle separation as viewed from the top. In the microfluidic channel, the direction of PN and PA is established at an angle of inclination (θ) to the direction of fluid flow. Samples were injected from the central inlet and focused by hydrodynamics. In the hybrid acoustic pressure channel resonating area, larger particles (red dots) and smaller particles (green dots) are separated because of the difference in the vertical displacement. F_r and F_d are the ARF and SDF, respectively.

microfluidic device: (1) the fabrication of IDTs on a lithium niobate ($LiNbO_3$) piezoelectric substrate and (2) the fabrication of the PDMS microchannel. The fabrication of IDTs involved photolithography, metal deposition, and lift-off processes. A layer of positive photoresist (SPR3012, MicroChem, USA) was first spin-coated on a 128° *Y*-cut *X*-propagation $LiNbO_3$ wafer, patterned with a UV light source, and then developed in a positive photoresist developer (AZ300 MIF, AZ Electronic Materials, USA). Plasma surface cleaning was applied before a double-layer metal (Ti/Al, 50 Å/1,500 Å) was deposited on the $LiNbO_3$ wafer using an e-beam evaporator (Semicore Corp.). Afterward, a lift-off process was followed to remove the photoresist, and a pair of identical IDTs were obtained.[53] This was followed by physical vapor deposition of a thick layer of 250 nm silicon dioxide, SiO_2, as a passivation layer. This SiO_2 layer not only enhances the bonding between the piezoelectric substrate and PDMS but also shields the electrode short circuit as well as fluid to prevent cross-contamination. In our setup, the width of the electrode finger and spacing gap of the IDTs were both set to 44 μm, corresponding to the SAW frequency of 22.725 MHz. The aperture of the IDTs was 6 mm, and the whole taSSAW device was 30 mm (length) × 30 mm (width) × 0.5 mm (height). The microstructure of the IDT and the surface vibration properties of the SAW device were measured (Figure S1 in the Supporting Information).

The PDMS microchannel with a width of 800 μm and a depth of 100 μm was fabricated using standard soft lithography and mould replica techniques. The silicon substrate for the microchannel mould was spin-coated by a photoresist (SU-8 2050, MicroChem, USA), followed by baking at 65 °C for 1 min and 95 °C for 4 min. After that, the silicon substrate was patterned with a UV light source and postexposure for 7 s at a light intensity of 16.8 mW/cm^2. The silicon wafers were baked again at 65 °C for 1 min and 95 °C for 4 min. Then, the silicon wafers were rinsed alternately in propylene glycol methyl ether acetate and isopropanol for 15 s until no white floccules floated off the surface. Then, the silicon wafers were dried with nitrogen and baked at 150 °C for 10 min. After obtaining a microchannel mould, a 1:10 mixture of a curing agent and a soft PDMS base (Sylgard 184 Silicone Elastomer clear, Ellsworth, USA) was degassed, cast on top of the microchannel mould, cured at 65 °C for 30 min, and peeled off. Finally, the IDT substrate and the PDMS microchannel were both treated with oxygen plasma to enhance their bonding strength, as shown in Figure 1B. The particles of interest were injected into the microchannel with polyethylene tubing (inner diameter: 1 mm). For the fabrication process of the above-mentioned SAW devices and microchannels, we have generated a flow chart (Figure S2 in the Supporting Information).

2.2. Experimental Setup. During the experiments, the fabricated acoustofluidic chip was positioned beneath a microscope (EX20, Soptop, China). The IDTs were interfaced with an amplifier (LZY-22+, Mini-circuits, USA) that modulates the radio frequency (RF) signals from a function generator (DSG3030, Rigol, China). A semiconductor chilling plate was used to dissipate the heat of the chip to avoid heating-related effects such as changes in fluid properties. The fluid flows, including two sheath fluids and one sample fluid, were controlled by individual syringe pumps (RSP01-BD, Biotaor, China) that were connected by polyethylene tubing with an inner diameter of 1 mm. Before the experiment, the hydrophobic reagent was flushed through the entire microchannel to prevent particles from sticking to the wall. Imaging was performed using a fluorescence camera, a high-speed camera, and a 4k high-definition camera on the microscope. The three cameras can meet the video needs for fluorescent particles, high-speed moving particles, and large-size particles and clearly record the movement behavior of the particles. The size distribution of the separated samples was tested with a nano-/micrometer particle size analyzer (NanoBrook 173Plus, Brookhaven, USA) and research-level dynamic light scattering analysis software. The acoustofluidic chips were positioned on a semiconductor chilling plate, and an upright microscope was used to monitor the experimental process. For deflection of the particles, a high-speed CCD camera was used to record the movement behavior of the particles at different flow rates, and ImageJ software (NIH, USA) was used for analysis. The separated target samples were collected from two PDMS channel outlets, each with 2 mL test tubes.

2.3. Sample Preparation. Different polystyrene (PS) particles, including red fluorescent PS particles (0.1 μm, Baseline, China), green fluorescent PS particles (0.5 μm, Baseline, China), blue fluorescent PS particles (1 μm, Baseline, China), nonfluorescent PS particles (1, 3, and 6 μm, Thermo Scientific, USA), and SiO_2 particles (750 nm, Sigma−Aldrich, USA), were suspended in deionized water containing 0.5% sodium dodecyl sulfate as samples. The flow rates of the obtained sample and two sheath fluids were set as 2, 2, and 6 μL/min, respectively, for hydrodynamic focusing. The separation purity and efficiency of the mixed particles were determined by flow cytometry. Pure samples were used to calibrate the setup and remove debris from the flow cytometry results. The ratio of each particle type is defined as the ratio of the corresponding number of particles detected by flow cytometry to the total number of particles counted. Separation efficiency is defined as the ratio of target particles separated from the mixed particles to all target particles. Likewise, the separation purity is defined as the ratio of the target particles

https://doi.org/10.1021/acsomega.2c04273
ACS Omega 2023, 8, 311−323

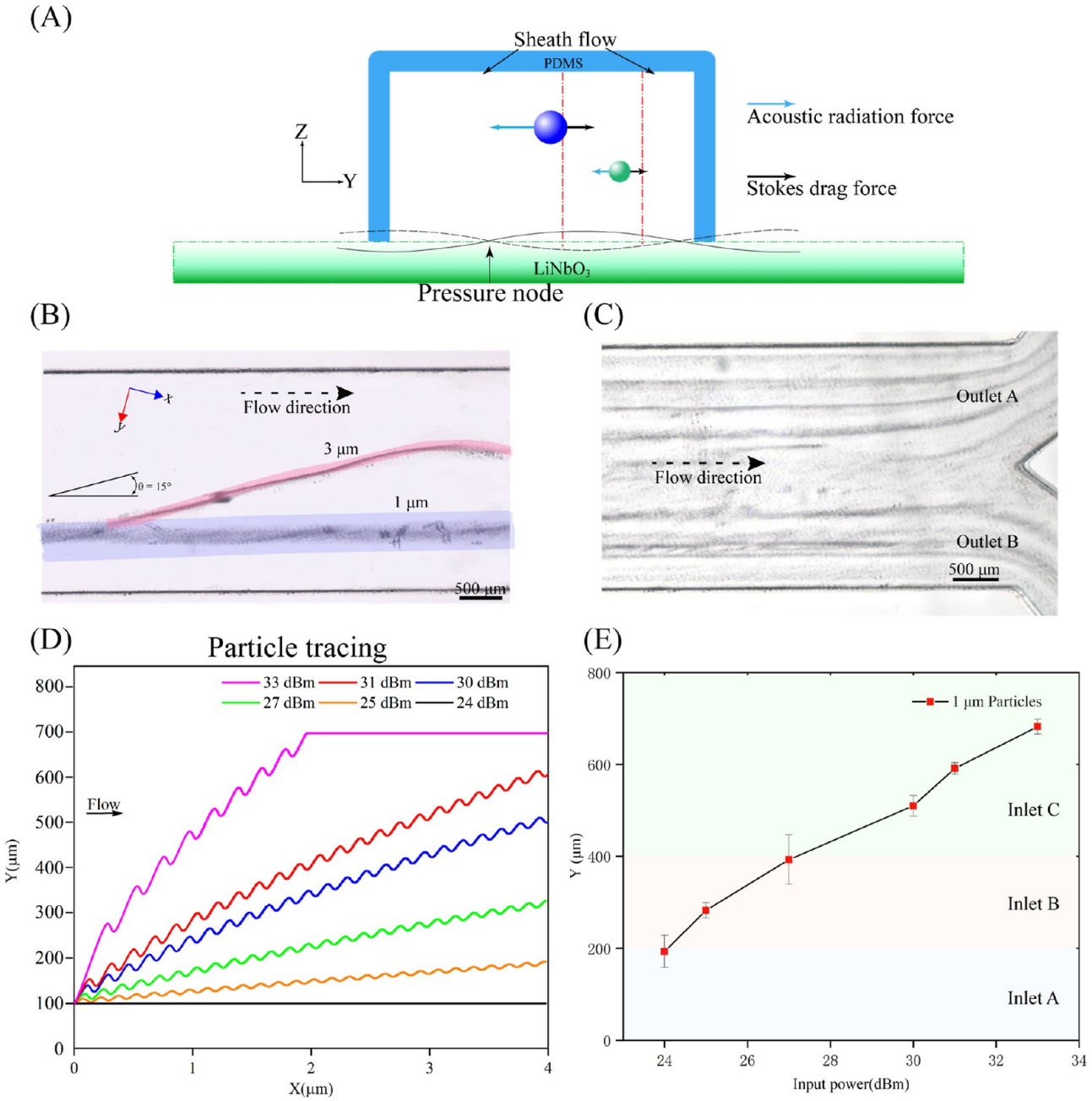

Figure 2. (A) Schematic illustration of the cross section of the two-dimensional taSSAW-based mechanism with respect to ARF and SDF. (B) Bright-field image of 1 μm particle and 3 μm particle separation. (C) Image of the outlet region showingthat the taSSAW field in the microchannel pushes 1 μm particles to each PN line. (D) Numerically calculated particle trajectories in the microchannel when subjected to different input powers. (E) Plot of deflection positions of 1 μm particles converging to PN lines in PDMS microchannels under different input powers. The data are presented as average ± standard error (n = 3). Scale bar: 500 μm.

separated to all particles separated from the same microchannel outlet.

3. RESEARCH ROUTE

When separating mixed particles, the optimization of control parameters must consider the balance of throughput and input power. Simply increasing one of the parameters and ignoring the other parameters will lead to a decrease in the separation purity and cannot satisfy the expected requirements. Therefore, the optimization strategy of the control parameters is essential. We will carry out parameter optimization analysis with respect to both numerical simulation and experimental research to achieve a better understanding of particle acoustophoretic motion and prediction of particle deflection trajectories from the physical level through numerical simulation. The influences of the control parameters on the particle deflection distance and the optimal parameter adjustment direction are determined through experiments. Finally, the effectiveness of this optimization strategy is verified in micron-scale separation and submicron-scale separation experiments.

4. RESULTS AND DISCUSSION

4.1. Mechanism of Particle Separation. A pair of IDTs with tilted angles generate two TSAWs propagating toward

https://doi.org/10.1021/acsomega.2c04273
ACS Omega 2023, 8, 311−323

each other. Due to the interference between the two TSAWs, taSSAW is generated and a periodic distribution of PNs and PAs is formed, which are tilted with respect to the direction of flow in the microchannel. The angle between the IDTs and the microfluidic channel is set to 15°.[49] The SSAWs cause periodic acoustic scattering of particles in the fluid within the microchannel, and acoustic pressure fluctuations generate ARF on the particles, pushing the particles to move to the PNs, as shown in Figure 1C. The ARF is described as

$$F_r = -\left(\frac{\pi p_0^2 V_p \beta_w}{2\lambda}\right)\varphi(\beta, \rho)\sin(2ky) \quad (1)$$

$$\varphi(\beta, \rho) = \frac{5\rho_p - 2\rho_m}{2\rho_p + \rho_m} - \frac{\beta_p}{\beta_w} \quad (2)$$

where p_0, λ, V_p, ρ_p, ρ_m, β_w, and β_p are the acoustic pressure, the acoustic wavelength, the particle volume, the density of the particle, the density of the medium, the compressibility of the medium, and the compressibility of the particle, respectively. In eq 1, y is the coordinate, as shown in Figure 1C, and k is the wavenumber of the SAW. Equation 2 describes the acoustic contrast factor φ, which determines whether a particle moves to a PN or PA in the SSAW field: the particles will aggregate at PN lines when φ is positive and at PA lines when φ is negative. Generally, most solid microspheres and cells in the aqueous solution have positive φ values (such as PS and SiO_2) and move toward PN lines in the SSAW field. The particle motion is impeded by the Stokes drag force (SDF), which is described as

$$F_d = -6\pi\mu R_p u_r \quad (3)$$

where μ, R_p, and u_r are the viscosity of the medium, the radius of the particle, and the relative velocity of the particle, respectively. From these formulas, we can determine that the magnitude of the ARF acting on a particle is a function of its radius, density, compressibility, and the power of the RF signal applied to the device. Therefore, the particles will experience varying ARF when these characteristics are different and can be separated in the SSAW device. Equation 3 illustrates that the F_d is proportional to the radius of a particle or cell, while eq 1 indicates that the ARF is proportional to the volume. Therefore, the ARF tends to limit the particles at the PN lines, whereas the SDF induced by the laminar flowing fluid pushes the particles forward along the flow direction. The separation mechanism in our experiment is based on the particle size, as shown in Figure 2A. When particles (cells) with different radii pass through the taSSAW area, these particles (cells) will experience ARF and ASF. For particles with a larger radius, the ARF dominates over the ASF, resulting in lateral displacement. In contrast, for particles with a small radius, the ASF dominates over the ARF, so the lateral displacement is small. When particles (cells) flow through the acoustic pressure field, the larger particles are deflected by the ARF, while the smaller particles cannot be deflected, thus realizing the separation of the mixed particles.

According to eq 1, a larger ARF is required for the deflection of submicron particles with a diameter of less than 1 μm. Therefore, we use a high-frequency SAW with a wavelength of 175 μm to enhance ARF, which corresponds to a resonant frequency of 22.725 MHz. In addition, higher power is utilized to further increase the amplitude of the acoustic pressure field. It should be noted that higher power will cause the chip to heat up, and the movement behavior of particles in the fluid will be affected by temperature, so a cooling plate is required to keep the system at a balanced temperature. Applying the taSSAW approach, we found that the separation purities of 1 and 3 μm PS microspheres can reach up to ∼94.3 and ∼92.6%, respectively. The separation process is observed in Figure 2B, where the larger 3 μm particles (marked in pink) are collected in the upper outlet A channel, while the smaller 1 μm particles (marked in blue) are accumulated in the lower outlet B channel.

Parametric research on the key variables in the design of acoustofluidic chips will improve the separation efficiency of microspheres of different sizes and enable better understanding of the particle separation mechanism based on taSSAW. We performed an analysis of the particle trajectory and particle motion behavior in a rectangular channel under the combined action of ARF and ASF using numerical simulations and finite element simulations (in the Supporting Information). The specific mechanism and key parameters of finite element analysis can be found in our previous research,[54] Nama's research,[55] or Taatizadeh's research,[56] which will not be repeated in this paper. We model the cross section of PDMS microchannels by finite element software to study fluid and particle motion within the microfluidic channel. In this 2D model, the width of the microchannel is equal to the wavelength length. The upper image in Figure S3 (in the Supporting Information) demonstrates the trajectory of 1 μm particles (Video S1 in the Supporting Information). Since ASF plays a leading role in the acoustic field, the particles are governed by the SDF and particle streaming vortices are generated. The lower image in Figure S3 (in the Supporting Information) displays the particle trajectory with a particle size of 3 μm (Video S2 in the Supporting Information). As the particle size increases, the ARF becomes more influential in the acoustic streaming field. The ARF pushes the particles out of the vortex toward the channel wall and the PN position (half wavelength). If the particle size is further increased, the vortex motion will almost completely vanish and the ARF will completely dominate the particle motion behaviour. The simulation results will be discussed in a later section in combination with the experiment.

4.2. Particle Acoustophoresis in PDMS Microchannels. Experiments were also conducted by using the taSSAW-based acoustofluidic chip to validate our simulation. First, we verified the effectiveness of the device. The entire PDMS microchannel was filled with 1 μm particles, and the particles were concentrated at the PN positions by the effect of SSAW. In laminar flow with a low Reynolds number, the particle motion presents linear aggregation, as shown in Figure 2D. The PS particles move uniformly along multiple PN lines, the interval between the lines is approximately half of one wavelength, and the acoustic pressure field distribution in the fluid domain conforms to the expected device design.

Second, we studied the particle trajectories under different acoustic powers (24, 25, 27, 30, 31, and 33 dBm) and selected particles with a diameter of 1 μm for this purpose. Figure 2E illustrates the simulated particle trajectories. The particle trajectories of different colours represent the numerical simulation results of different powers. The initial position of the beads ahead of the taSSAW working area is distributed in the range of 100 μm in the Y direction. For the trajectory of the particle when the input power is 24 dBm, since the ARF is

https://doi.org/10.1021/acsomega.2c04273
ACS Omega 2023, 8, 311−323

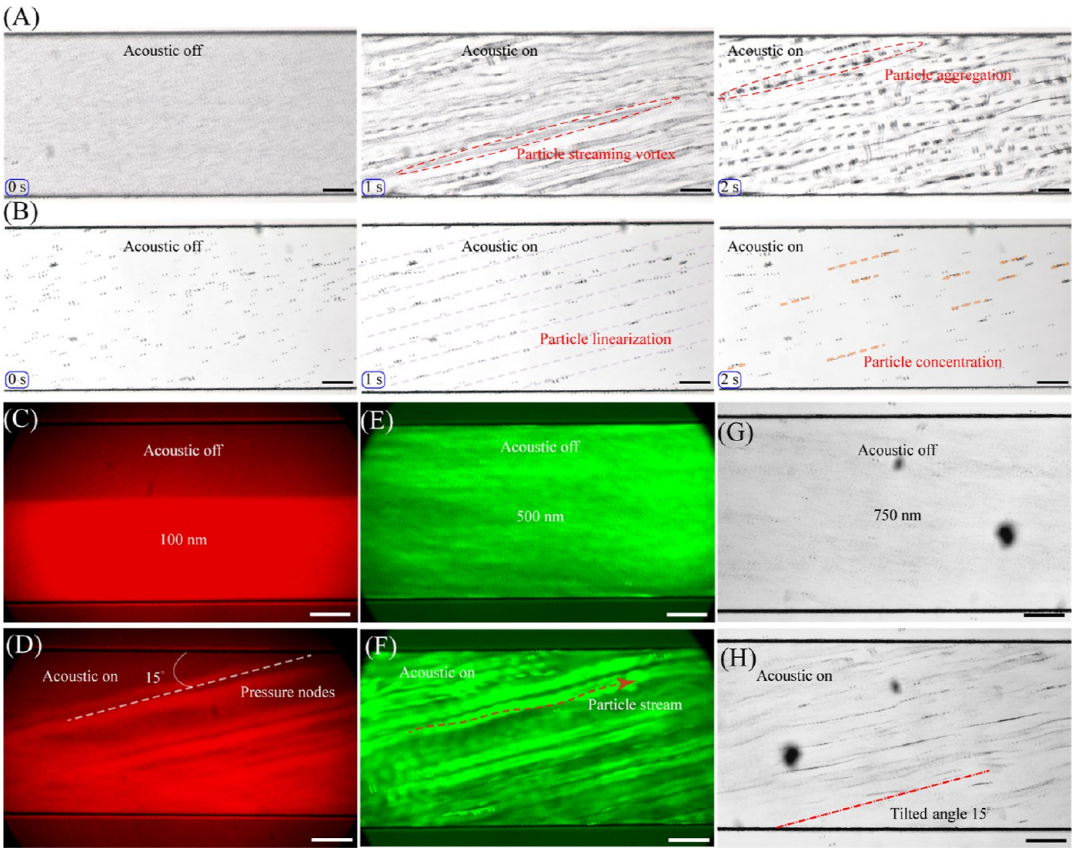

Figure 3. Different particle deflection sizes in the taSSAW-based field. (A) 1 μm PS particles are deflected by the taSSAW acoustic field, and the particle stream occurs. (B) 6 μm PS particles converge to the PN lines and gradually concentrate. (C) Fluorescence images of 100 nm PS particles with the taSSAW acoustic field turned off and (D) the taSSAW acoustic field turned on. (E) Fluorescence images of 500 nm PS particles with the taSSAW acoustic field turned off and (F) the taSSAW acoustic field turned on. The 500 nm PS particle stream is affected by ASF. (G) Fluorescence images of 750 nm SiO_2 particles with the taSSAW acoustic field turned off. (H) 750 nm SiO_2 particles converge to PN lines under the effect of ARF. Scale bar: 500 μm.

much weaker than the streaming-induced ASF, the particle almost follows the original undisturbed streamline. As the input power increases, the impact of the ARF on the particles becomes stronger, overcomes the restriction of the viscous drag on the particles, transitions to the vertical flow velocity direction, and crosses one or more PN lines. When the force of the particles in the *Y*-direction reaches dynamic equilibrium, the final particle trajectory converges to narrow lines parallel to the direction of the flow. For an input power of 33 dBm, the particle trajectory converges in advance in the *X*-direction. We also conducted a series of experiments to explore the influence of particle size on particle trajectory. The trajectories of particles of different sizes at the same input power are also numerically calculated (Figure S3 in the Supporting Information).

Finally, we verify the simulation results through experiments, and the results show that the simulation model again matches well with the experimental results. Figure 2F shows the deflection position of 1 μm particles converging to the PN lines in the PDMS microchannel under different input powers. The sheath flow is introduced from inlet A and inlet C, and the sample particles are introduced from inlet B. The flow rates of inlet A, inlet B, and inlet C are 2, 2, and 6 μL/min, respectively. The initial position of the particles is distributed between 200 and 320 μm (*Y* direction) in the microchannel. For input powers of 24 and 25 dBm, the particle positions are distributed in the PN lines in the lower half of the microchannel and the particles are collected from outlet B. For an input power of 27 dBm, a few particles move to the upper half of the microchannel, which means that some particles will be collected from outlet A. When the input power is greater than 30 dBm, almost all 1 μm particles are deflected to the upper half of the microchannel and flow out from outlet A. Therefore, for the 1 μm particles, the critical power of the microchannel exit deflection (outlet A) that occurs at the preset flow rate is 27 dBm. It should be noted that this power is only achieved for the device parameters we designed.

4.3. Particle Deflection by a taSSAW-Based Acousto-fluidic Chip. Our method of separating micrometer and submicrometer particles is based on the difference in particle size. We explored the deflection of particles of different sizes in the microchannel under constant power input. Figure 3A shows the deflection of 1 μm particles by an acoustic field. The 1 μm particles are first filled in the entire microchannel, and the input power of taSSAW is fixed at 27 dBm. The particles quickly form the particle streaming at the position of the PN lines: that is, the vortex streaming. We recorded the vortex motion of the particles with a high-speed camera (Videos S3 and S4 in the Supporting Information), which effectively verifies the finite element simulation results. When the acoustic field lasts for 2 s, the particles are concentrated into clusters (particle aggregation) and large clusters of particles are arranged along the line of PNs. Figure 3B shows the linear arrangement of 6 μm particles in the acoustic field. The 6 μm

https://doi.org/10.1021/acsomega.2c04273
ACS Omega 2023, 8, 311−323

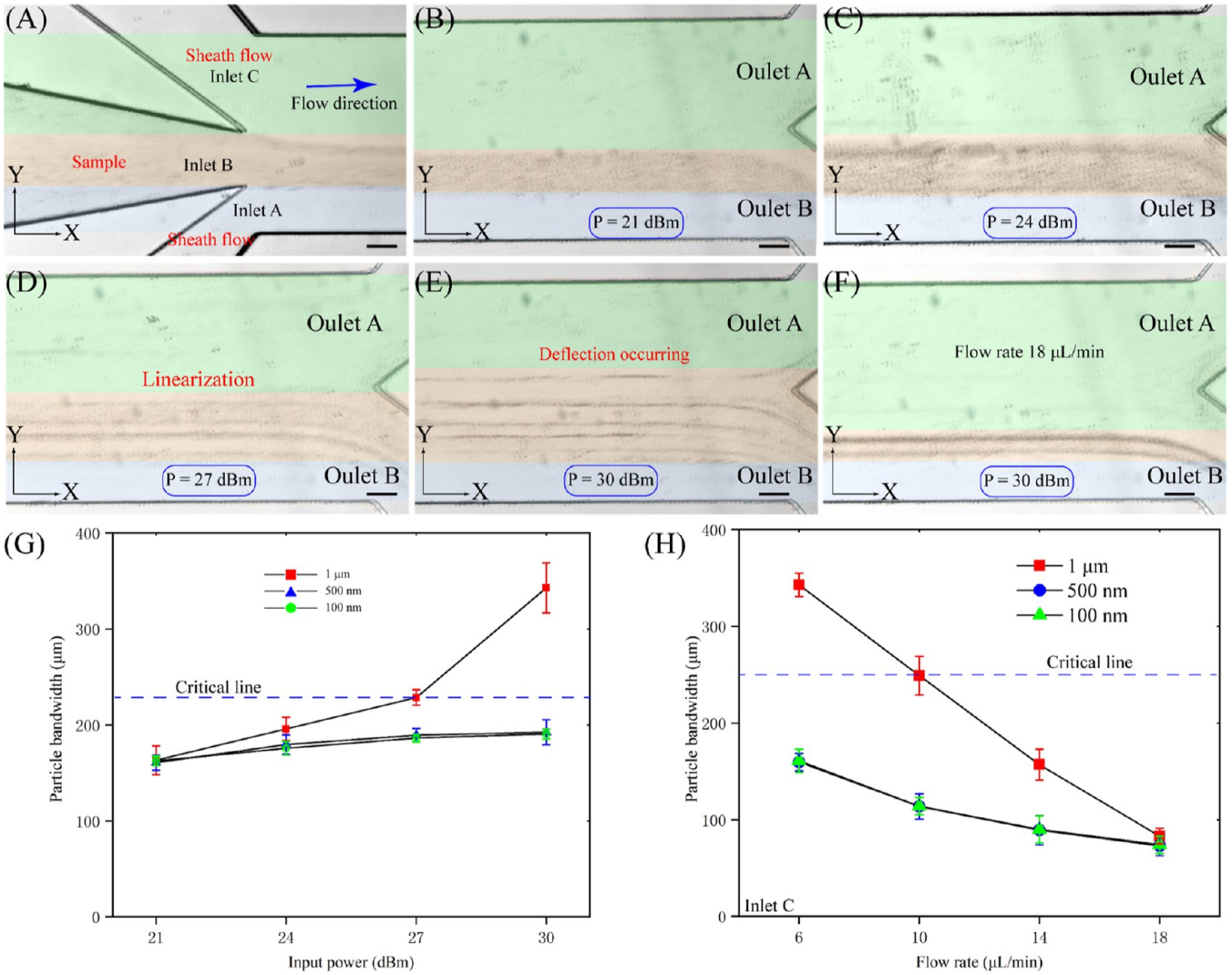

Figure 4. Deflection trajectory of 1 μm particles in the acoustofluidic chip. (A) Bright-field image of the inlet region of the microchannel. The sheath flow enters from inlet A and inlet C, and the sample particles enter from inlet B. The laminar flow width of the inlets is marked with different colors. The CMOS high-speed camera recorded the bright-field image of the 1 μm particle trajectory in the outlet area. The sheath flow and sample particle flow rates are 6, 2, and 2 μL/min, respectively. The input powers of the chip are (B) 21, (C) 24, (D) 27, and (E) 30 dBm. (F) Flow rates of the sheath flow and samples are 18, 6, and 6 μL/min, and the input power is 30 dBm. (G) Plot of the correlation between PBW and input power for particles of different sizes (n = 3). (H) Plot of the correlation between PBW and flow rate for particles of different sizes. The four sets of flow rates are (1) 6, 2, and 2 μL/min; (2) 10, 3.3, and 3.3 μL/min; (3) 14, 4.7, and 4.7 μL/min; and (4) 18, 6, and 6 μL/min. The abscissa represents the flow rate of inlet C. The data are presented as average ± standard error (n = 3). Scale bar: 500 μm.

particles quickly converge to the PN line from the original position by ARF (Video S5 in the Supporting Information). The effect of ASF is limited, so it cannot induce movement of large particles through vortex streaming. However, the combined force of ASF and ARF makes the particles gradually concentrate together. Figure 3C–F shows the fluorescence images of 100 nm particles and 500 nm particles in the acoustic pressure region of the microchannel with the acoustic field turned off and the acoustic field turned on, respectively. According to eq 1, 100 nm particles are slightly affected by ARF. To observe the positions of the particles in the microchannel more clearly after deflection, we poured the particles only into the lower half of the microchannel at a slow flow rate of 0.1 μL/min, as shown in Figure 3C. When the input power is increased to 30 dBm, some particles will be deflected under ARF, but there are still a large number of particles that are not deflected in the lower half of the microchannel, as shown in Figure 3D. Compared with the 100 nm particle behaviour, at the same input power, 500 nm particles are dominated by a stronger ARF and the deflection of particles in the microchannel is more obvious; moreover, this is accompanied by the particle streaming phenomenon, as shown in Figure 3F. Figure 3G,H displays the bright-field images of 750 nm SiO_2 particles in the acoustic pressure region of the microchannel with the taSSAW turned off and turned on, respectively. The large ARF experienced by the 750 nm SiO_2 particles results from the significantly larger acoustic contrast factor compared to the PS particles (φ is 0.437 for PS and 1.786 for SiO_2), and the particles show better linear convergence on the PN lines.

We experimentally validated that the acoustofluidic chip we designed can provide a strong ARF. When the input power is sufficiently large, even 100 nm particles can be deflected by the taSSAW acoustic field. As shown by eqs 1, 3, and S5, the

https://doi.org/10.1021/acsomega.2c04273
ACS Omega 2023, 8, 311−323

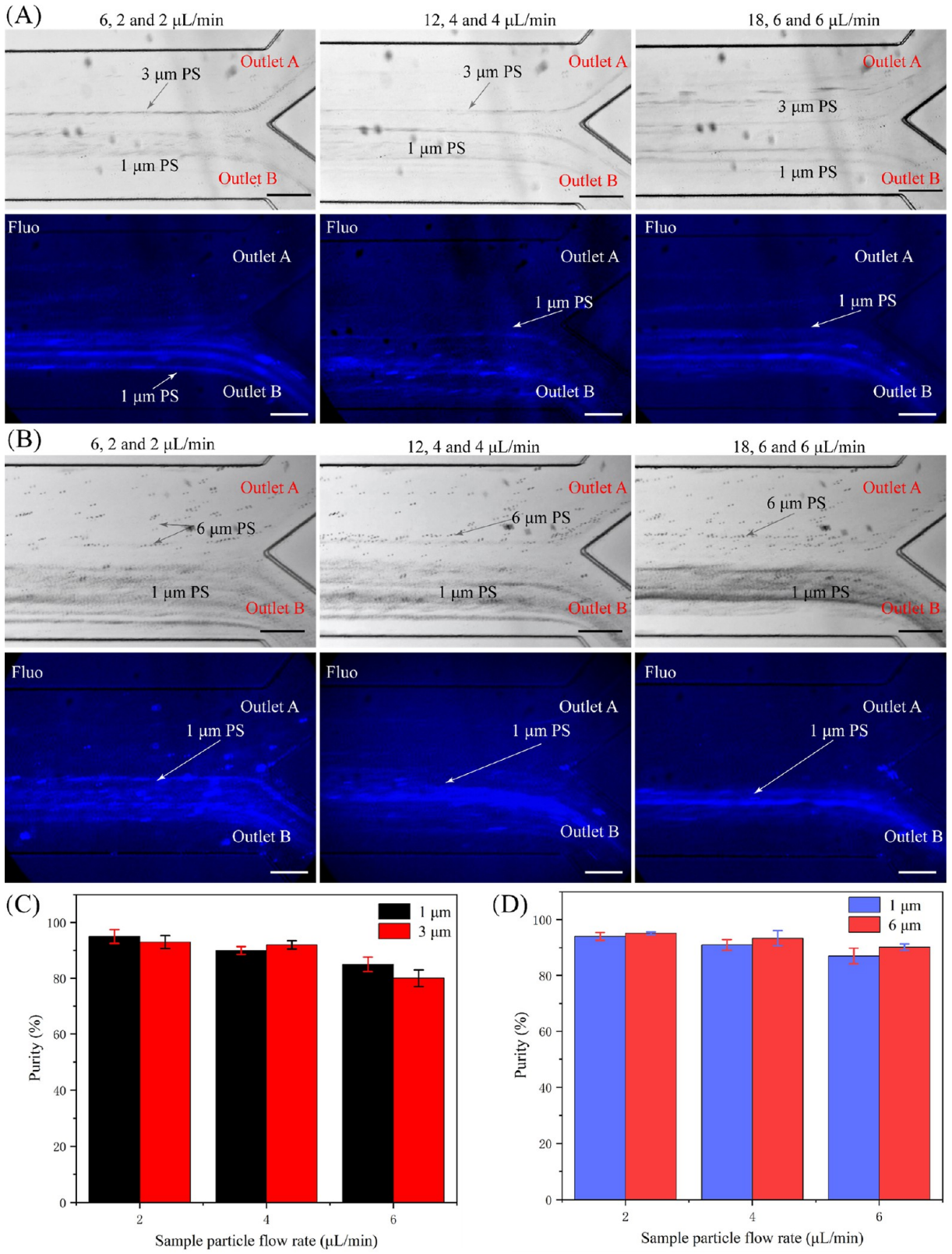

Figure 5. Bright-field and fluorescence field images of acoustic separation of micron-sized particles in a continuous fluid. (A) Images of the separation of 1 μm PS particles and 3 μm PS particles in the outlet area of the microchannel. (B) Images of the separation of 1 μm PS particles and 6 μm PS particles in the outlet area of the microchannel. The flow rates in these combinations are 6, 2, and 2 μL/min; 12, 4, and 4 μL/min; and 18, 6, and 6 μL/min from left to right. Separation performance for (C) 1 and 3 μm particles and (D) 1 and 6 μm particles. The purity of the collected particles was determined. The data are presented as average ± standard error (n = 3). Scale bar: 500 μm.

dominant roles of ASF and ARF on the particles in the acoustofluidic system can be switched by adjusting the flow rate and the input power of the device to manipulate the particles to achieve deflection according to the set path.

https://doi.org/10.1021/acsomega.2c04273
ACS Omega 2023, 8, 311−323

4.4. Correlation of Deflection Position with Input Power and Flow Rate. The wider microchannel design can not only increase the throughput of particle manipulation (sorting or separation) but also make the particles distributed on multiple PN lines, which causes some particles to escape from the predetermined collection channel and reduces the particle separation efficiency. To determine the optimal operating parameters, we studied the correlation between the particle deflection position, acoustic power, and particle flow rate. Outside the acoustic activity area, that is, the outlet area of the microchannel, the position of the particles in the Y direction no longer changes. The particle's position was recorded by a high-speed camera system under different conditions. Figure 4A shows a bright-field image of sample particles and sheath flow at the inlet of the microchannel. Green and blue marks show the area of the microchannel where the sheath flow is located, and orange marks show the area of the microchannel where the particles are located. The sheath flow and sample flow rates were 6 μL/min (green), 2 μL/min (blue), and 2 μL/min (orange). The particle diameter is 1 μm.

Figure 4B−E shows bright-field images of 1 μm particles in the outlet region when the input powers are 21, 24, 27, and 30 dBm, respectively. The longitudinal width of the fluid domain where the particles are located is called the particle bandwidth (PBW). When the input power is continuously increased, the particles undergo two changes in the fluid domain. The first is the physical phenomenon of the laminar flow where the particles are located. Due to the effect of ARF, the particles gradually converge to the PN line, resulting in obvious particle linearization. The second is the deflection position of the particle. Due to the strong ARF provided by the high power, the particles cross multiple PN lines. The Y-direction displacement of the fluid domain where the particles are located increases (orange mark); that is, the width of the PBW increases, bringing a portion of the particles out of outlet A, as shown in Figure 4E. Upon increase of the flow rate of the sheath flow and sample particles to 18 μL/min (green mark), 6 μL/min (orange mark), and 6 μL/min (blue mark), the input power remained at 30 dBm. Although the particles still exhibited obvious linearization, which is specifically manifested as convergence to two PN lines, the width of the PBW was reduced, resulting in particle collection only at outlet B, as shown in Figure 4F. This experimental phenomenon demonstrates that when separating two kinds of particles, the dynamic balance of flow rate and input power needs to be considered in the design parameters. To achieve high throughput and high separation purity, the flow rate can be appropriately increased while increasing the power to prevent one kind of particle from flowing out of the two outlets.

Figure 4G shows a plot of the PBW as a function of the input power for 100, 500, and 1 μm PS particles. The flow rates of the sheath flow and sample particles are 6, 2, and 2 μL/min, respectively. For 1 μm particles, as the input power increases, PBW first slowly increases between 150 and 220 μm; however, when the input power reaches 27 dBm, the maximum deflection position of 1 μm particles is close to the centerline of outlet A and outlet B (critical line), and once surpassing this power, the PBW jumps to ∼350 μm. At this time, the maximum deflection position has crossed the critical line, removing some particles from outlet A. This is because, at this input power, ARF maximizes the deflection distance of the particle trajectory. For the maximum deflection distances of 100 and 500 nm particles, neither reached the critical value within the range of experimental conditions. The reason for this is that particles with smaller sizes are much less affected by ARF than are larger particles. Figure 4H shows a plot of the PBW as a function of the flow rate for 100 nm, 500 nm, and 1 μm PS particles, with an input power of 30 dBm. To ensure that particles can be collected from outlet B in the initial state, the flow rate ratio of inlet A, inlet B, and inlet C is 3:1:1. Note that the flow rate setting is related to the inlet width of the microchannel we designed and can be changed according to the design parameters of the microchannel. The experimental results show that with the increase in the flow rate of inlet C, the PBW decreases greatly. When the inlet C flow rate is greater than 10 μL/min, no particles will be brought out from outlet A. For the particles of 100 and 500 nm, the PBW decreases slowly and the particles always move away from outlet A. The results show that when the particle size increases, the ARF increases more quickly than the ASF, so for submicron particles, the ARF has less impact than for 1 μm particles. The deflection of submicron particles requires a larger input power to increase the effect of ARF, while the deflection of micron particles is relatively easy to achieve.

4.5. Acoustic Separation of Micron Particles and Submicron Particles. We have demonstrated that the taSSAW device is capable of micron and submicron particle deflection based on particle size and input power, but to further investigate the separation performance of the taSSAW device, we adjusted the input power and flow rate to separate (1) 3 μm PS particles and 1 μm PS particles, (2) 6 μm PS particles and 1 μm PS particles, (3) 1 μm PS particles and 100 nm PS particles, and (4) SiO_2 particles and 100 nm PS particles. The separation strategy is based on the difference in the acoustic contrast factor φ of the two kinds of particles so that the ARF of the particles is significantly different in a continuous fluid. The first sheath flow (inlet A) for sample focusing has the same flow rate as the sample flow (inlet B), and the second sheath flow (inlet C) for sample transfer is 3 times the sample flow rate. For example, values of 6, 2, and 2 μL/min were applied for the second sheath flow, sample flow, and first sheath flow, respectively. At the same time, the acoustic wave intensity is enhanced to ensure sufficient lateral displacement of larger particles.

Figure 5 shows bright-field and fluorescence images of the outlet region at different flow rates. Figure 5A demonstrates the separation of 3 μm PS particles and 1 μm PS particles (Video S6 in the Supporting Information). Figure 5B displays the separation of 6 μm PS particles and 1 μm PS particles (Video S7 in the Supporting Information). The expected result was that the larger 3 and 6 μm particles would be collected from outlet A under the effect of the acoustic field, while the smaller 1 μm particles would be collected from outlet B and would remain close to the original stream. We collected 10 μL samples from outlet A and outlet B when SSAWs were activated. The size distribution of the samples was measured using a Brookhaven multiangle particle size analyzer (NanoBrook 173Plus, Brookhaven Instruments Ltd, USA) based on the DLS method. Sample particle counts were measured using a flow cytometer (Cytoflex, Beckman, USA). The same volume of the original sample was also measured as a control. The sample particle flow rate was increased from 2 to 6 μL/min. At the same time, the sheath flow rate was increased from 6 to 18 μL/min. Generally, the deflection for the particles induced by ARF decreased as the flow rate increased. At flow rates of 6, 2,

https://doi.org/10.1021/acsomega.2c04273
ACS Omega 2023, 8, 311−323

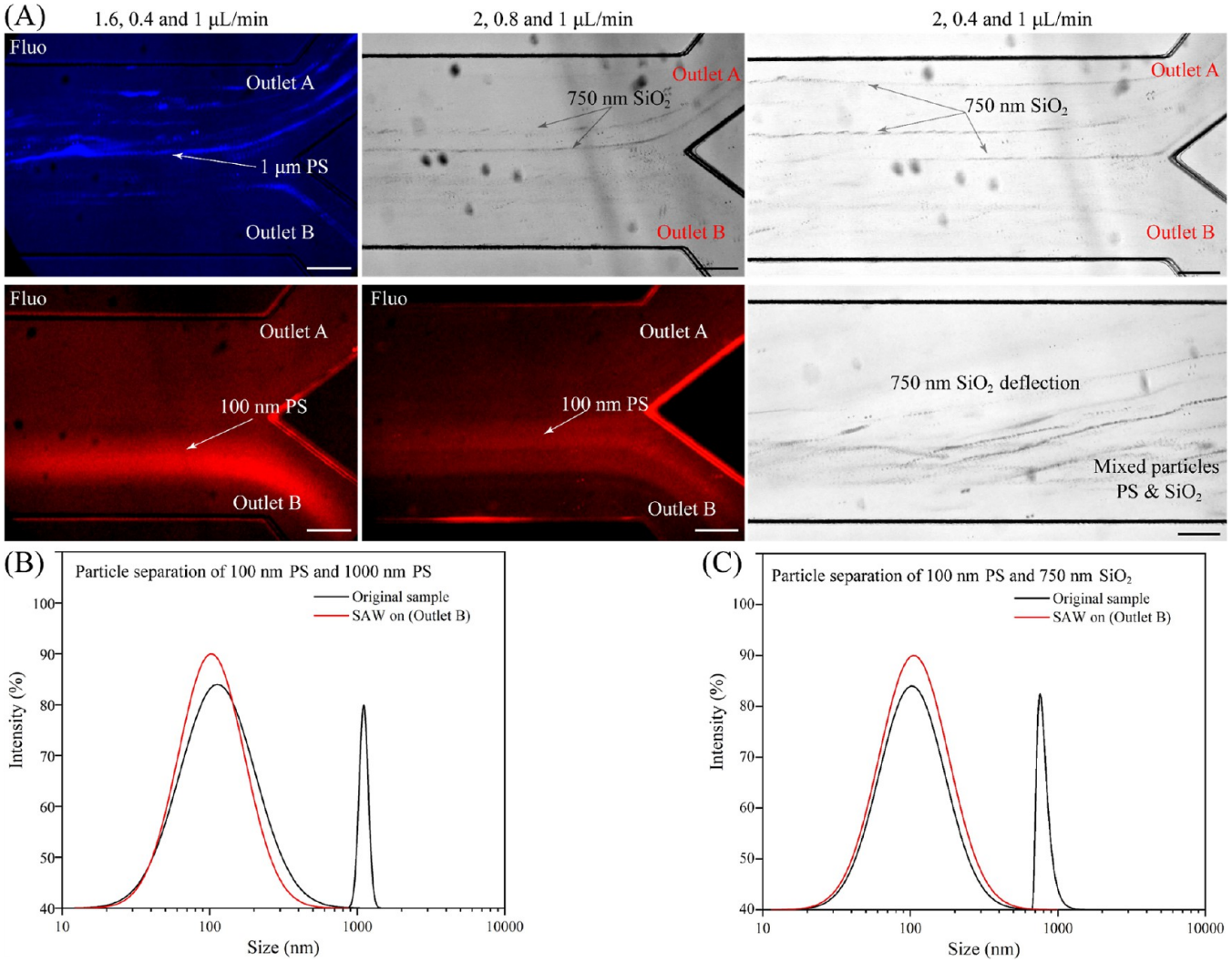

Figure 6. Bright-field and fluorescence field images of acoustic separation of submicron particles in a continuous fluid. (A) Bright-field and fluorescence field images for the separation of 100 nm PS particles and 1 μm PS particles and 750 nm SiO_2 particles and 100 nm PS particles. Scale bar: 500 μm. Size distribution of sample particles and collected particles for (B) 1 μm PS particles and 100 nm PS particles and (C) 750 nm SiO_2 particles and 100 nm PS particles. Size distribution of samples before (black line) and after taSSAW-based acoustic separation (red line). Each sample is analyzed by DLS technology for particle size, and the lognormal size distribution image of particle size is obtained. The acoustic-based submicron particle separation technique filters larger particles and determines the detected sample size in outlet B, in which only one peak exists in the size domain distribution.

and 2 μL/min, most of the larger particles (3 μm in Figures 5A, 6 μm in Figure 5B) were deflected from the mixed particles and separated from the 1 μm particles. The device was effective even when the flow rates were increased to 18, 6, and 6 μL/min, although a few larger particles were found in the sample collected at outlet B. We performed particle size measurements (Figures S4 and S5 in the Supporting Information) and quantified the original samples and separated samples. The purity of the collected samples was characterized by dividing the target particle number by the number of total particles, and the results are shown in Figure 5C,D. In independent separation experiments, greater than 80% purity was obtained for both 1 and 6 μm particle separation and 1 and 3 μm particle separation. The maximum separation purity of 3 μm particles and 1 μm particles was 93.1 and 94.2%, respectively, and the maximum separation efficiency was 94.5 and 93.4%, respectively. The maximum separation purity of 6 μm particles and 1 μm particles was 95.7 and 94.8%, respectively, and the maximum separation efficiency was 96.6 and 95.1%, respectively (Table S2 in the Supporting Information). Notably, when the flow rate is increased, there is also a significant decrease in the purity level. The results demonstrate that the peak resolution of the samples processed by the acoustofluidic chip is higher in the size domain; furthermore, the obtained separated sample particles have higher purity.

The separation of submicron-scale particles also becomes feasible using our taSSAW device. We demonstrated the separation of 100 nm PS particles and 1 μm PS particles, as well as the separation of 750 nm SiO_2 particles and 100 nm PS particles, as shown in Figure 6A. According to the effects of ARF and ASF on particle separation, the input power (corresponding to ARF) and flow rate (corresponding to ASF) of the device were optimized. The optimal input power for the separation of 100 nm PS particles and 1 μm PS particles was 31.3 dBm when the flow rates were 1.6, 0.4, and 1 μL/min. When the flow rates were 2, 0.8, and 1 μL/min, the optimal input power for the separation of 750 nm SiO_2 particles and 100 nm PS particles was 30.8 dBm. Figure 6A also shows the

https://doi.org/10.1021/acsomega.2c04273
ACS Omega 2023, 8, 311−323

deflection of 750 nm SiO_2 particles in the acoustic pressure field region when 750 nm SiO_2 particles and 100 nm PS particles are separated, and the sample flow rate is reduced to 0.4 μL/min. When SiO_2 particles are affected by ARF, the deflection trajectories increase, resulting in an increase in the longitudinal deflection distance of SiO_2 particles in the outlet region. In previous submicron particle separation SSAW devices, researchers used designed IDTs with reflector gratings or IDTs with oblique angles. The device used in this work differs from previous designs in that it enhances ARFs through a double direct-type IDT design.

We also performed particle size testing on submicron particle-blended samples versus isolated samples. The results are shown in Figure 6B. The abscissa represents the size distribution, the ordinate is the optical intensity in the corresponding size range, and the optical intensity is determined by the number of particles. Each original mixed sample contains two distinct peaks at their respective constituent particle sizes. The DLS technique used in the Brookhaven particle size analyzer has defects in peak resolution due to discrete particle size distributions. On the other hand, the separated samples processed by our acoustofluidic chip showed only one peak in the size domain and the optical intensity of this peak was larger than that of the original sample. Specifically, the purities of the separated particles of 100 nm and 1 μm were 93.6 and 90.1%, respectively, and the corresponding efficiencies were 86.3 and 83.7%, respectively, when the flow rates were 1.6, 0.4, and 1 μL/min. When the flow rates were 2, 0.8, and 1 μL/min, the purities of the separated particles at 750 and 100 nm were 89.7 and 91.2% and the corresponding efficiencies were 84.1 and 80.2%, respectively. When the flow rate of the sheath flow remained unchanged and the flow rate of the sample particles was reduced to 0.4 μL/min, the purities of the separated particles at 750 and 100 nm were 93.4 and 92.3% and the corresponding efficiencies were 89.5 and 88.6%, respectively (Table S3 in the Supporting Information). For the separation of submicron particles, since they are less affected by ARF, the purity level of the target particles can be increased by appropriately reducing the sample flow rate. The results showed that the larger particles were filtered by the separation device and only the smaller particles were present in the separated sample. In previous studies, Huang's team attempted to separate particles and cells using a taSSAW-based device, with separation purity ranging from 84 to 98% and separation efficiency (yield) from 82 to 97%. Table S4 (in the Supporting Information) provides a general trend for the taSSAW-based method in terms of yield, purity, and throughput (flow rate) for a given object size. In our separation experiments, the separation purity was 80 to 95% and the separation efficiency (yield) was 83 to 97%. These results indicate that our acoustofluidic separation device can achieve separation performance comparable to Huang's taSSAW device and offers the potential for practical applications.

5. CONCLUSIONS

In this work, we developed an acoustofluidic platform (chip) by bonding a PDMS microchannel at a tilted angle of 15° to an SSAW device coated with a SiO_2 film. We then demonstrated a taSSAW acoustic field in the microchannel by deflecting 1 μm PS particles in the acoustic pressure field and concentrating on the PN lines. The acoustic streaming field was simulated by finite element simulation, and the trajectory of particles in the microchannel was simulated by numerical calculation. The simulation results were verified by experiments. The experimental results exhibit good agreement with our established particle motion model. The correlation of input power and flow rate with respect to particle trajectories is indicated by the deflection distances of particles with different particle sizes, from which we derive an optimization strategy for particle separation.

By optimizing the control parameters for particle separation, we separated micron and submicron particles based on the acoustofluidic chip. The experimental results show that in the wide range of 100−6 μm, particles with large size differences, such as 1 and 6 μm, can be separated. The 100 nm particles and 750 nm particles can also be separated, indicating that the device has the ability to separate submicron particles. We characterized the separation purity by particle size analysis and flow cytometry, and the test results demonstrated the good controllability and sensitivity of our device. This technology is label-free, efficient, and versatile, providing an acoustic separation method for biological and clinical medical applications such as cell and bacterial sorting and sample purification.

■ ASSOCIATED CONTENT

Supporting Information

The Supporting Information is available free of charge at https://pubs.acs.org/doi/10.1021/acsomega.2c04273.

More detailed numerical simulation of the particle separation process of the acoustofluidic platform; description of the fabricated process, device, simulation results and particle size test; and information on particle separation characteristics (PDF)

Finite element simulation of 1 μm particle dominated by ASF to form a particle streaming vortex (MP4)

Finite element simulation of 6 μm particles moving to the PN by the dominant action of ARF (MP4)

1 μm particles forming a particle streaming vortex under the effect of taSSAW (MP4)

500 nm particles forming a particle streaming vortex under the effect of taSSAW (MP4)

6 μm particle deflection under taSSAW (MP4)

3 μm particles separated in a mixed stream of 1 and 3 μm particles (MP4)

6 μm particles separated in a mixed stream of 1 and 6 μm particles (MP4)

■ AUTHOR INFORMATION

Corresponding Authors

Hong Hu − *School of Mechanical Engineering and Automation, Harbin Institute of Technology, Shenzhen 518055, China;* orcid.org/0000-0002-7443-0885; Email: honghu@hit.edu.cn

Chen Fu − *College of Physics and Optoelectronic Engineering, Shenzhen University, Shenzhen 518055, China;* Email: chenfu@szu.edu.cn

Authors

Junlong Han − *School of Mechanical Engineering and Automation, Harbin Institute of Technology, Shenzhen 518055, China*

https://doi.org/10.1021/acsomega.2c04273
ACS Omega 2023, 8, 311−323

Yulin Lei − *School of Mechanical Engineering and Automation, Harbin Institute of Technology, Shenzhen 518055, China*
Qingyun Huang − *Shenzhen Polytechnic, Shenzhen 518055, China*
Chenhui Gai − *School of Mechanical Engineering and Automation, Harbin Institute of Technology, Shenzhen 518055, China*
Jia Ning − *School of Mechanical Engineering and Automation, Harbin Institute of Technology, Shenzhen 518055, China*

Complete contact information is available at: https://pubs.acs.org/10.1021/acsomega.2c04273

Author Contributions

J.H. designed this research. C.F. fabricated the microchannel and bonded the SSAW device. J.H. and Y.L. conducted the experiments and analyzed the data. H.H. and J.H. prepared the manuscript. Q.H. helped with the finite element simulation. J.N. and C.G. conducted the particle separation experiment. H.H. and C.F. supervised the research.

Notes

The authors declare no competing financial interest.

■ ACKNOWLEDGMENTS

The authors are grateful for the financial support of the National Natural Science Foundation of China (NSFC) under grant s52175532 and 11974252 and Shenzhen Science and Technology Research and Development Fund Grants JSGG20201201100410029, JSGG20201201100401004, and SGDX20190919102801693.

■ REFERENCES

(1) Gonzalez-Hidalgo, M.; Guerrero-Pena, F. A.; Herold-Garcia, S.; Jaume-i-Capo, A.; Marrero-Fernandez, P. D. Red Blood Cell Cluster Separation From Digital Images for Use in Sickle Cell Disease. *IEEE J. Biomed. Health Inform.* **2015**, *19*, 1514−1525.
(2) Chen, X.; Zhang, S.; Gan, Y.; Liu, R.; Wang, R.; Du, K. Understanding microbeads stacking in deformable Nano-Sieve for Efficient plasma separation and blood cell retrieval. *J. Colloid Interface Sci.* **2022**, *606*, 1609−1616.
(3) Wang, Z.; Wang, H.; Becker, R.; Rufo, J.; Yang, S.; Mace, B. E.; Wu, M.; Zou, J.; Laskowitz, D. T.; Huang, T. J. Acoustofluidic separation enables early diagnosis of traumatic brain injury based on circulating exosomes. *Microsyst. Nanoeng.* **2021**, *7*, 20.
(4) Fraser, A. G.; Kamath, R. S.; Zipperlen, P.; Martinez-Campos, M.; Sohrmann, M.; Ahringer, J. Functional genomic analysis of C. elegans chromosome I by systematic RNA interference. *Nature* **2000**, *408*, 325−330.
(5) Tung, Y. C.; Hsiao, A. Y.; Allen, S. G.; Torisawa, Y. S.; Ho, M.; Takayama, S. High-throughput 3D spheroid culture and drug testing using a 384 hanging drop array. *Analyst* **2011**, *136*, 473−478.
(6) Xie, Y.; Bachman, H.; Huang, T. J. Acoustofluidic methods in cell analysis. *TrAC, Trends Anal. Chem.* **2019**, *117*, 280−290.
(7) Salafi, T.; Zeming, K. K.; Zhang, Y. Advancements in microfluidics for nanoparticle separation. *Lab Chip* **2016**, *17*, 11−33.
(8) Nam, J.; Lim, H.; Kim, D.; Jung, H.; Shin, S. Continuous separation of microparticles in a microfluidic channel via the elasto-inertial effect of non-Newtonian fluid. *Lab Chip* **2012**, *12*, 1347.
(9) Didar, T. F.; Li, K.; Veres, T.; Tabrizian, M. Separation of rare oligodendrocyte progenitor cells from brain using a high-throughput multilayer thermoplastic-based microfluidic device. *Biomaterials* **2013**, *34*, 5588−5593.
(10) Collins, D. J.; Alan, T.; Neild, A. Particle separation using virtual deterministic lateral displacement (vDLD). *Lab Chip* **2014**, *14*, 1595−1603.
(11) Shen, S.; Tian, C.; Li, T.; Xu, J.; Chen, S.; Tu, Q.; Yuan, M.; Liu, W.; Wang, J. Spiral microchannel with ordered micro-obstacles for continuous and highly-efficient particle separation. *Lab Chip* **2017**, *17*, 3578−3591.
(12) Lee, K. H.; Kim, S. B.; Lee, K. S.; Sung, H. J. Enhancement by optical force of separation in pinched flow fractionation. *Lab Chip* **2011**, *11*, 354−357.
(13) Sollier, E.; Rostaing, H.; Pouteau, P.; Fouillet, Y.; Achard, J. Passive microfluidic devices for plasma extraction from whole human blood. *Sens. Actuators, B* **2009**, *141*, 617−624.
(14) Dash, S.; Mohanty, S. Dielectrophoretic separation of micron and submicron particles: A review. *Electrophoresis* **2014**, *35*, 2656−2672.
(15) Baresch, D.; Thomas, J.; Marchiano, R. Observation of a Single-Beam Gradient Force Acoustical Trap for Elastic Particles: Acoustical Tweezers. *Phys. Rev. Lett.* **2016**, *116*, 024301.
(16) Droz, X.; Harraghy, N.; Lançon, E.; Le Fourn, V.; Calabrese, D.; Colombet, T.; Liechti, P.; Rida, A.; Girod, P.; Mermod, N. Automated microfluidic sorting of mammalian cells labeled with magnetic microparticles for those that efficiently express and secrete a protein of interest. *Biotechnol. Bioeng.* **2017**, *114*, 1791−1802.
(17) Orloff, N. D.; Dennis, J. R.; Cecchini, M.; Schonbrun, E.; Rocas, E.; Wang, Y.; Novotny, D.; Simmonds, R. W.; Moreland, J.; Takeuchi, I.; et al. Manipulating particle trajectories with phase-control in surface acoustic wave microfluidics. *Biomicrofluidics* **2011**, *5*, 44107−441079.
(18) Ding, X.; Lin, S. C.; Lapsley, M. I.; Li, S.; Guo, X.; Chan, C. Y.; Chiang, I. K.; Wang, L.; McCoy, J. P.; Huang, T. J. Standing surface acoustic wave (SSAW) based multichannel cell sorting. *Lab Chip* **2012**, *12*, 4228−4231.
(19) Guldiken, R.; Jo, M. C.; Gallant, N. D.; Demirci, U.; Zhe, J. Sheathless Size-Based Acoustic Particle Separation. *Sensors* **2012**, *12*, 905−922.
(20) Dalili, A.; Samiei, E.; Hoorfar, M. A review of sorting, separation and isolation of cells and microbeads for biomedical applications: microfluidic approaches. *Analyst* **2019**, *144*, 87−113.
(21) Lenshof, A.; Laurell, T. Continuous separation of cells and particles in microfluidic systems. *Chem. Soc. Rev.* **2010**, *39*, 1203.
(22) Antfolk, M.; Laurell, T. Continuous flow microfluidic separation and processing of rare cells and bioparticles found in blood—A review. *Anal. Chim. Acta* **2017**, *965*, 9−35.
(23) Destgeer, G.; Lee, K. H.; Jung, J. H.; Alazzam, A.; Sung, H. J. Continuous separation of particles in a PDMS microfluidic channel via travelling surface acoustic waves (TSAW). *Lab Chip* **2013**, *13*, 4210.
(24) Collins, D. J.; Ma, Z.; Han, J.; Ai, Y. Continuous micro-vortex-based nanoparticle manipulation via focused surface acoustic waves. *Lab Chip* **2016**, *17*, 91−103.
(25) Ma, Z.; Collins, D. J.; Ai, Y. Detachable Acoustofluidic System for Particle Separation via a Traveling Surface Acoustic Wave. *Anal. Chem.* **2016**, *88*, 5316−5323.
(26) Jo, M. C.; Guldiken, R. Active density-based separation using standing surface acoustic waves. *Sens. Actuators, A* **2012**, *187*, 22−28.
(27) Ma, Z.; Collins, D. J.; Guo, J.; Ai, Y. Mechanical Properties Based Particle Separation via Traveling Surface Acoustic Wave. *Anal. Chem.* **2016**, *88*, 11844−11851.
(28) Destgeer, G.; Jung, J. H.; Park, J.; Ahmed, H.; Park, K.; Ahmad, R.; Sung, H. J. Acoustic impedance-based manipulation of elastic microspheres using travelling surface acoustic waves. *RSC Adv.* **2017**, *7*, 22524−22530.
(29) Fakhfouri, A.; Devendran, C.; Ahmed, A.; Soria, J.; Neild, A. The size dependant behaviour of particles driven by a travelling surface acoustic wave (TSAW). *Lab Chip* **2018**, *18*, 3926−3938.
(30) Skowronek, V.; Rambach, R. W.; Schmid, L.; Haase, K.; Franke, T. Particle Deflection in a Poly(dimethylsiloxane) Microchannel Using a Propagating Surface Acoustic Wave: Size and Frequency Dependence. *Anal. Chem.* **2013**, *85*, 9955−9959.

(31) Ung, W. L.; Mutafopulos, K.; Spink, P.; Rambach, R. W.; Franke, T.; Weitz, D. A. Enhanced surface acoustic wave cell sorting by 3D microfluidic-chip design. *Lab Chip* **2017**, *17*, 4059−4069.
(32) Wang, Y.; Wang, Y.; Mei, D.; Yu, Z.; Xue, D. Standing surface acoustic wave-assisted fabrication of patterned microstructures for enhancing cell migration. *Bio-Des. Manuf.* **2020**, *3*, 87−97.
(33) Tayebi, M.; Yang, D.; Collins, D. J.; Ai, Y. Deterministic Sorting of Submicrometer Particles and Extracellular Vesicles Using a Combined Electric and Acoustic Field. *Nano Lett.* **2021**, *21*, 6835−6842.
(34) Wu, M.; Ozcelik, A.; Rufo, J.; Wang, Z.; Fang, R.; Jun Huang, T. Acoustofluidic separation of cells and particles. *Microsyst. Nanoeng.* **2019**, *5*, 32.
(35) Devendran, C.; Gralinski, I.; Neild, A. Separation of particles using acoustic streaming and radiation forces in an open microfluidic channel. *Microfluid. Nanofluid.* **2014**, *17*, 879−890.
(36) Fornell, A.; Nilsson, J.; Jonsson, L.; Periyannan Rajeswari, P. K.; Joensson, H. N.; Tenje, M. Controlled Lateral Positioning of Microparticles Inside Droplets Using Acoustophoresis. *Anal. Chem.* **2015**, *87*, 10521−10526.
(37) Collins, D. J.; Neild, A.; Ai, Y. Highly focused high-frequency travelling surface acoustic waves (SAW) for rapid single-particle sorting. *Lab Chip* **2016**, *16*, 471−479.
(38) Fakhfouri, A.; Devendran, C.; Collins, D. J.; Ai, Y.; Neild, A. Virtual membrane for filtration of particles using surface acoustic waves (SAW). *Lab Chip* **2016**, *16*, 3515−3523.
(39) Ren, L.; Chen, Y.; Li, P.; Mao, Z.; Huang, P.; Rufo, J.; Guo, F.; Wang, L.; McCoy, J. P.; Levine, S. J.; et al. A high-throughput acoustic cell sorter. *Lab Chip* **2015**, *15*, 3870−3879.
(40) Nguyen, T. D.; Tran, V. T.; Fu, Y. Q.; Du, H. Patterning and manipulating microparticles into a three-dimensional matrix using standing surface acoustic waves. *Appl. Phys. Lett.* **2018**, *112*, 213507.
(41) Han, J. L.; Hu, H.; Huang, Q. Y.; Lei, Y. L. Particle separation by standing surface acoustic waves inside a sessile droplet. *Sens. Actuators, A* **2021**, *326*, 112731.
(42) Ai, Y.; Sanders, C. K.; Marrone, B. L. Separation of Escherichia coli Bacteria from Peripheral Blood Mononuclear Cells Using Standing Surface Acoustic Waves. *Anal. Chem.* **2013**, *85*, 9126−9134.
(43) Sriphutkiat, Y.; Zhou, Y. Particle Accumulation in a Microchannel and Its Reduction by a Standing Surface Acoustic Wave (SSAW). *Sensors* **2017**, *17*, 106.
(44) Destgeer, G.; Ha, B. H.; Park, J.; Jung, J. H.; Alazzam, A.; Sung, H. J. Microchannel Anechoic Corner for Size-Selective Separation and Medium Exchange via Traveling Surface Acoustic Waves. *Anal. Chem.* **2015**, *87*, 4627−4632.
(45) Zhao, S.; Wu, M.; Yang, S.; Wu, Y.; Gu, Y.; Chen, C.; Ye, J.; Xie, Z.; Tian, Z.; Bachman, H.; et al. A disposable acoustofluidic chip for nano/microparticle separation using unidirectional acoustic transducers. *Lab Chip* **2020**, *20*, 1298−1308.
(46) Wu, M.; Mao, Z.; Chen, K.; Bachman, H.; Chen, Y.; Rufo, J.; Ren, L.; Li, P.; Wang, L.; Huang, T. J. Acoustic Separation of Nanoparticles in Continuous Flow. *Adv. Funct. Mater.* **2017**, *27*, 1606039.
(47) Wu, M.; Ouyang, Y.; Wang, Z.; Zhang, R.; Huang, P.; Chen, C.; Li, H.; Li, P.; Quinn, D.; Dao, M.; et al. Isolation of exosomes from whole blood by integrating acoustics and microfluidics. *Proc. Natl. Acad. Sci. U.S.A.* **2017**, *114*, 10584−10589.
(48) Ayan, B.; Ozcelik, A.; Bachman, H.; Tang, S.; Xie, Y.; Wu, M.; Li, P.; Huang, T. J. Acoustofluidic coating of particles and cells. *Lab Chip* **2016**, *16*, 4366−4372.
(49) Ding, X.; Peng, Z.; Lin, S. C. S.; Geri, M.; Li, S.; Li, P.; Chen, Y.; Dao, M.; Suresh, S.; Huang, T. J. Cell separation using tilted-angle standing surface acoustic waves. *Proc. Natl. Acad. Sci. U.S.A.* **2014**, *111*, 12992−12997.
(50) Li, P.; Mao, Z.; Peng, Z.; Zhou, L.; Chen, Y.; Huang, P.; Truica, C. I.; Drabick, J. J.; El-Deiry, W. S.; Dao, M.; et al. Acoustic separation of circulating tumor cells. *Proc. Natl. Acad. Sci. U.S.A.* **2015**, *112*, 4970−4975.
(51) Wu, M.; Huang, P. H.; Zhang, R.; Mao, Z.; Chen, C.; Kemeny, G.; Li, P.; Lee, A. V.; Gyanchandani, R.; Armstrong, A. J.; et al. Circulating Tumor Cell Phenotyping via High-Throughput Acoustic Separation. *Small* **2018**, *14*, 1801131.
(52) Winkler, A.; Brünig, R.; Faust, C.; Weser, R.; Schmidt, H. Towards efficient surface acoustic wave (SAW)-based microfluidic actuators. *Sens. Actuators, A* **2016**, *247*, 259−268.
(53) Han, J.; Yang, F.; Hu, H.; Huang, Q.; Lei, Y.; Li, M. Thermal Control Design and Packaging for Surface Acoustic Wave Devices in Acoustofluidics. *IEEE Trans. Ultrason. Ferroelectr. Freq. Control* **2022**, *69*, 386−398.
(54) Huang, Q.-Y.; Hu, H.; Lei, Y.-L.; Han, J.-L.; Zhang, P.; Dong, J. Simulation and experimental investigation of surface acoustic wave streaming velocity. *Jpn. J. Appl. Phys.* **2020**, *59*, 064001.
(55) Nama, N.; Barnkob, R.; Mao, Z.; Kähler, C. J.; Costanzo, F.; Huang, T. J. Numerical study of acoustophoretic motion of particles in a PDMS microchannel driven by surface acoustic waves. *Lab Chip* **2015**, *15*, 2700−2709.
(56) Taatizadeh, E.; Dalili, A.; Rellstab-Sánchez, P. I.; Tahmooressi, H.; Ravishankara, A.; Tasnim, N.; Najjaran, H.; Li, I. T. S.; Hoorfar, M. Micron-sized particle separation with standing surface acoustic wave—Experimental and numerical approaches. *Ultrason. Sonochem.* **2021**, *76*, 105651.

https://doi.org/10.1021/acsomega.2c04273
ACS Omega 2023, 8, 311−323